ADVANCED FUNCTIONAL MATERIALS

Supporting Information

for *Adv. Funct. Mater.*, DOI 10.1002/adfm.202312188

Swimmable Micro-Battery for Targeted Power Delivery

Pengzhou Li, Zhe Yang, Chuanfa Li, Jiaxin Li, Chuang Wang, Jiawei Chen, Sijia Yu, Yanan Zhang, Yi Jiang, Yue Gao, Bingjie Wang and Huisheng Peng**

Supporting Information

Swimmable Micro-Battery for Targeted Power Delivery

Pengzhou Li, Zhe Yang, Chuanfa Li, Jiaxin Li, Chuang Wang, Jiawei Chen, Sijia Yu, Yanan Zhang, Yi Jiang, Yue Gao, Bingjie Wang, and Huisheng Peng**

P. Li, Z. Yang, Dr. C. Li, J. Li, C. Wang, J. Chen, S. Yu, Dr. Y. Zhang, Y. Jiang, Prof. Y. Gao, Prof. B. Wang, Prof. H. Peng
*State Key Laboratory of Molecular Engineering of Polymers, Department of Macromolecular Science, Institute of Fiber Materials and Devices, and Laboratory of Advanced Materials, Fudan University, Shanghai 200438, China. *E-mail: wangbingjie@fudan.edu.cn; penghs@fudan.edu.cn.*

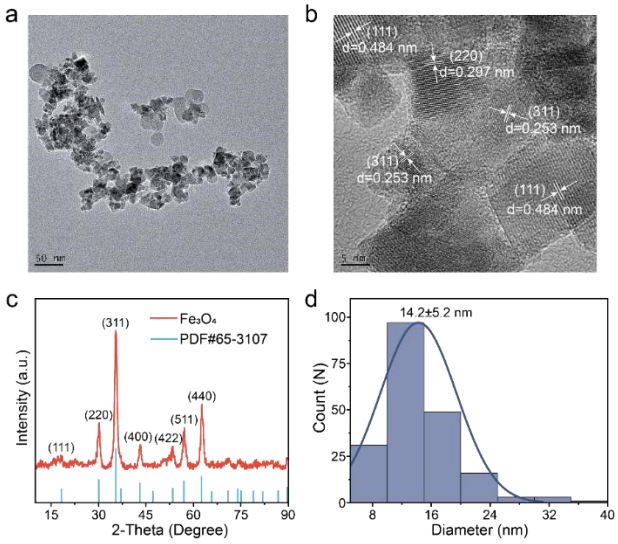

Figure S1. Characterization of the synthesized magnetic Fe_3O_4 nanoparticles. (**a**, **b**) Transmission electron microscopic images at low and high magnifications, respectively. (**c**, **d**) X-ray diffraction pattern and corresponding particle size distribution, respectively. n=200.

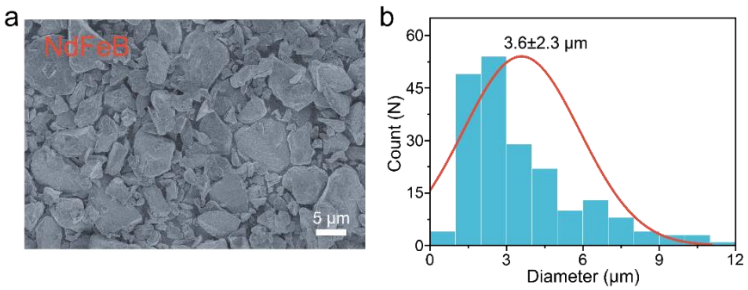

Figure S2. (**a**, **b**) Scanning electron microscopic image of the NdFeB magnetic particles and corresponding particle size distribution, respectively. n=200.

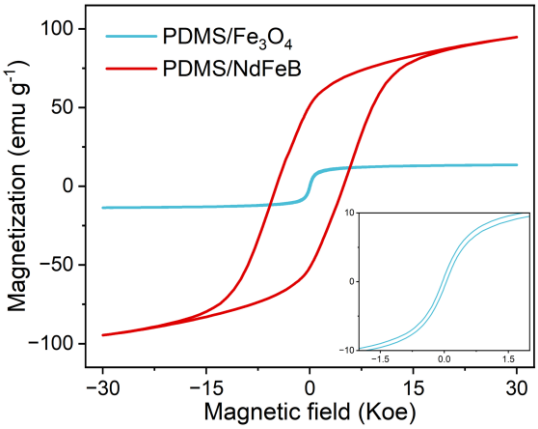

Figure S3. Hysteresis loops of PDMS/NdFeB and PDMS/Fe_3O_4 composites with residual magnetizations of 51.7 and 0.75 emu g^{-1}, respectively.

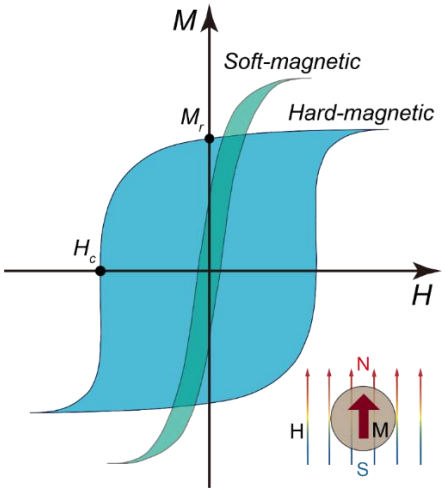

Figure S4. Typical magnetization curves with magnetic hysteresis loops of soft-magnetic and hard-magnetic materials.

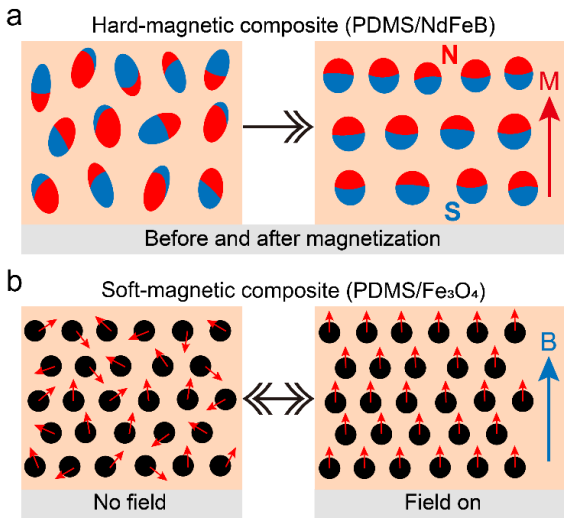

Figure S5. Two-dimensional schematics of the mechanism of (**a**) PDMS/NdFeB hard-magnetic composite before and after being magnetized by an impulse magnetic field. The red arrow marks the direction of the magnetization. (**b**) PDMS/Fe_3O_4 soft-magnetic composite under an external magnetic field. The red and blue arrows indicate the polarization directions of internal magnetic particles and the applied external magnetic field, respectively.

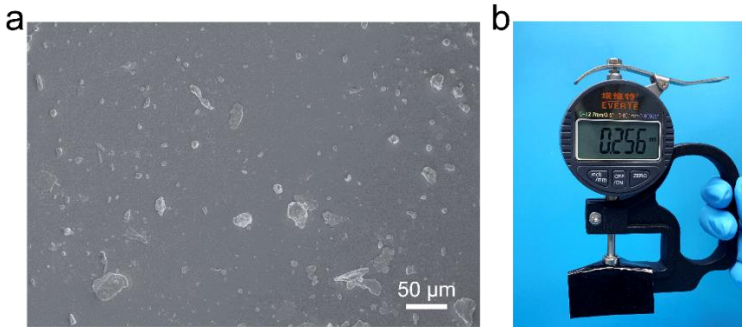

Figure S6. (**a, b**) Scanning electron microscopic image and photograph showing thickness of soft-magnetic PDMS/Fe_3O_4 composite film, respectively.

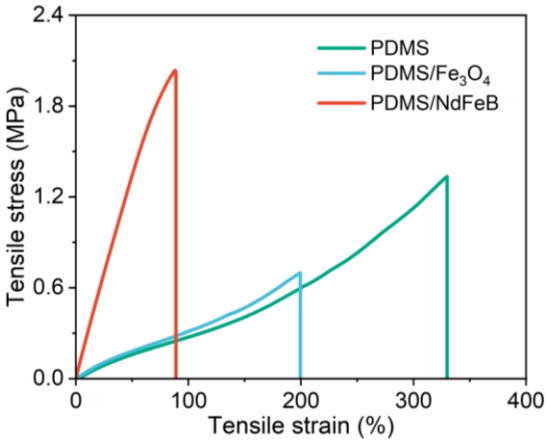

Figure S7. Tensile stress-strain curves of magnetic composites.

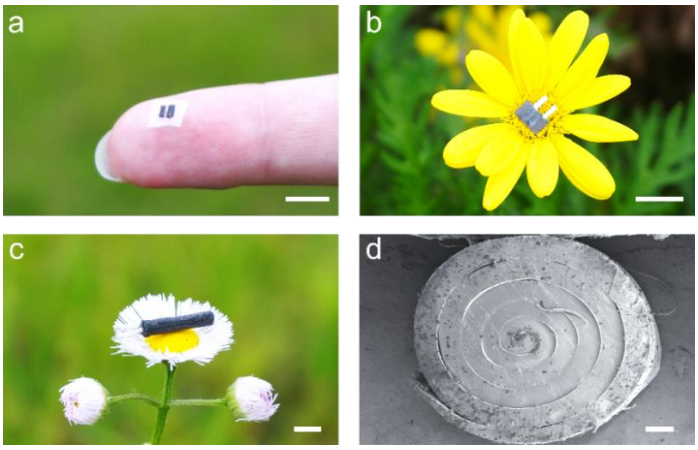

Figure S8. Photographs of the printed MBs at planar states with (**a**) PET substrate lying on the finger and (**b**) PDMS/Fe_3O_4 flexible substrate lying on the flower. (**c**) Photograph of a swimmable MB lying on a flower. (**d**) Side view of the scanning electron microscopic image of a rolled-up MB. Scale bars, 1 cm for (**a**, **b**), 2 mm for (**c**), and 200 μm for (**d**).

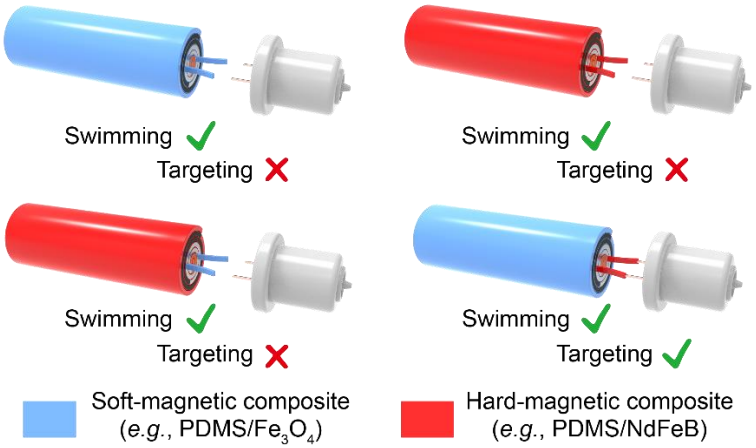

Figure S9. Four different combination modes of soft and hard-magnetic composites for substrates and tabs.

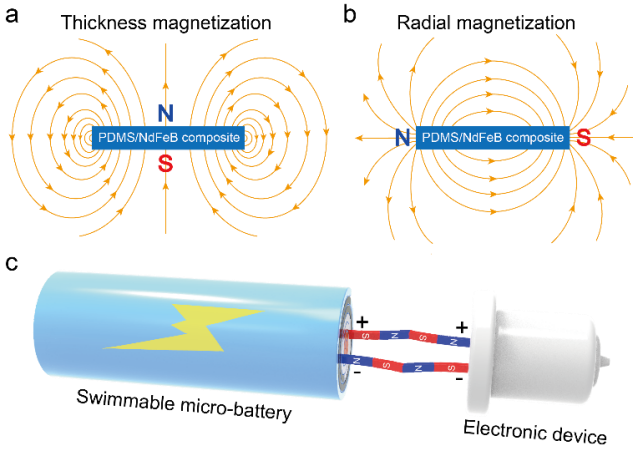

Figure S10. (**a**, **b**) Magnetic field distribution diagram of the PDMS/NdFeB hard magnetic composite after (**a**) thickness and (**b**) radial magnetization. (**c**) A schematic diagram illustrating the correct connection between a swimmable micro-battery and an electronic device through the interaction of the opposite magnetic poles (North and South poles), with radial magnetization along the PDMS/NdFeB hard-magnetic composite.

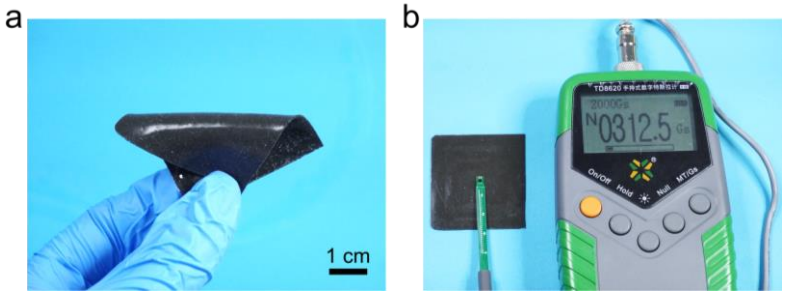

Figure S11. (**a**) Photograph of the PDMS/NdFeB composite (the mass ratio of NdFeB to PDMS is 4:1) and (**b**) a magnetic field intensity of 312.5 Gs (or 31.25 mT) detected by the Gauss meter.

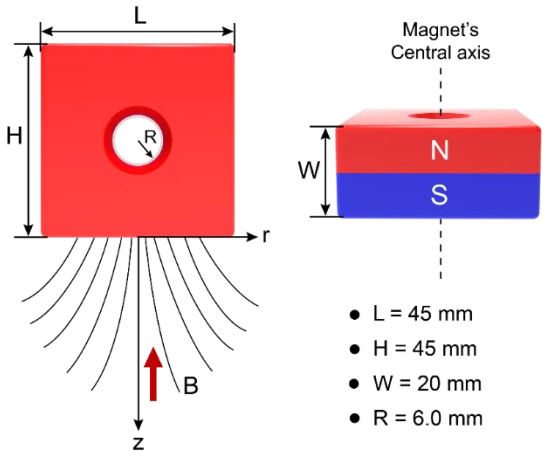

Figure S12. Schematic of the cuboid permanent magnet for remotely actuating swimmable MBs.

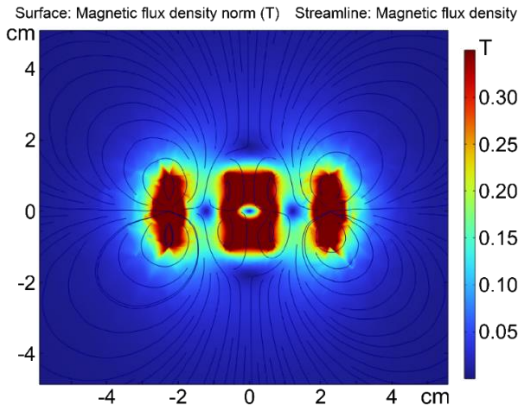

Figure S13. The magnetic field distribution around the cuboid permanent magnet.

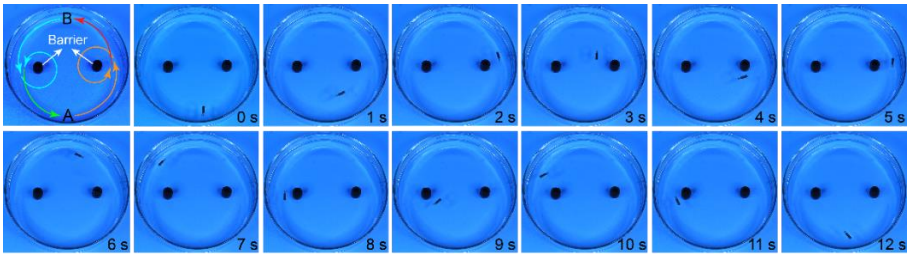

Figure S14. Experimental demonstration of the swam along a specified complex route (A-B-A) under the action of an external magnetic field. Magnetic fields for actuation

(about 8 mT) were generated by a cuboid permanent magnet at a distance of 5 cm.

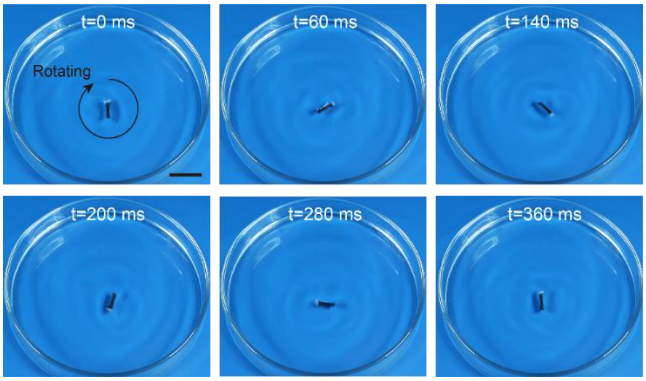

Figure S15. Quantitative characterization of the responsiveness of the swimmable MB. The swimmable MB completed a rotation cycle within 360 ms under the action of a rotating magnetic field (7.5 mT, 400 rpm). Scale bar: 1 cm.

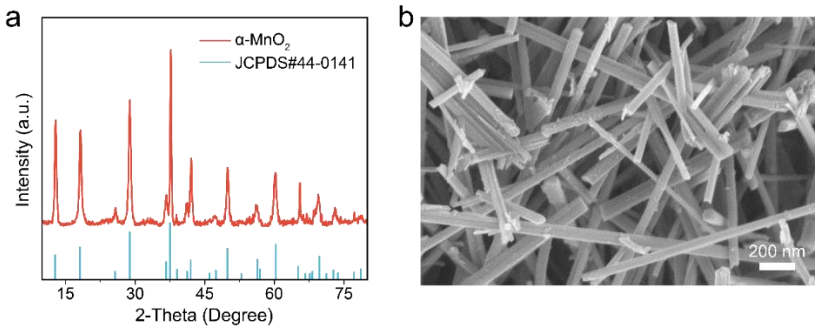

Figure S16. (**a**) X-ray diffraction pattern and (**b**) scanning electron microscopic image of the synthesized α-MnO_2 nanorods for cathode materials.

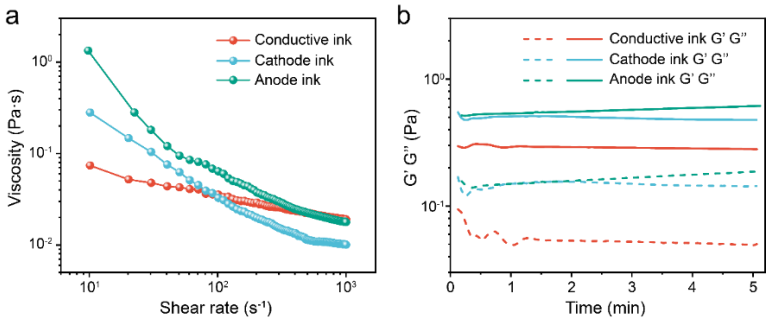

Figure S17. Rheological characterizations of the electrode inks for printing MBs. (**a**) Apparent viscosity as a function of shear rate for carbon-based conductive, cathode, and anode inks. (**b**) Storage modulus (G') and loss modulus (G'') as a function of time for carbon-based conductive, cathode, and anode inks.

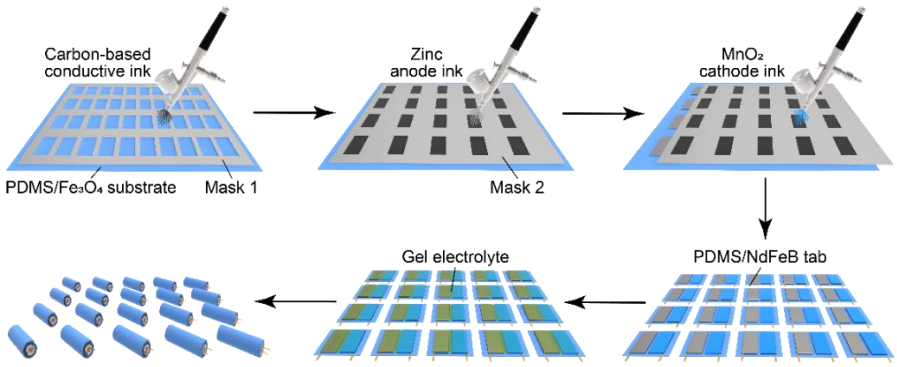

Figure S18. Diagram of the scalable preparation of swimmable MBs *via* spray printing.

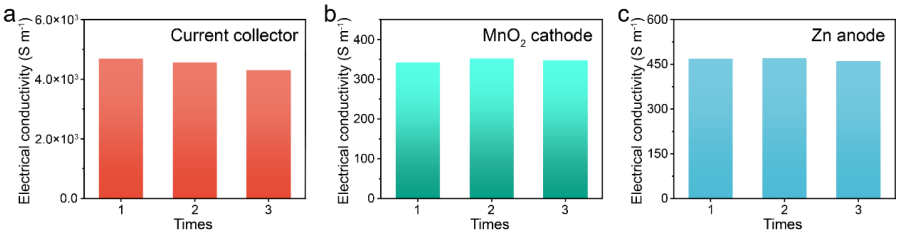

Figure S19. Electrical conductivities of the printed electrode films on PET substrate. (**a**) Carbon-based current collector, (**b**) MnO_2 cathode, and (**c**) Zn anode.

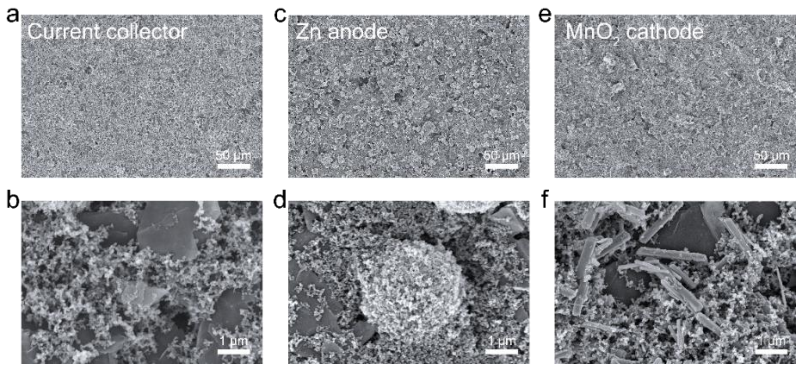

Figure S20. Scanning electron microscopic images of the printed (**a**, **b**) carbon-based current collector, (**c**, **d**) Zn anode, and (**e**, **f**) MnO_2 cathode at low and high magnifications.

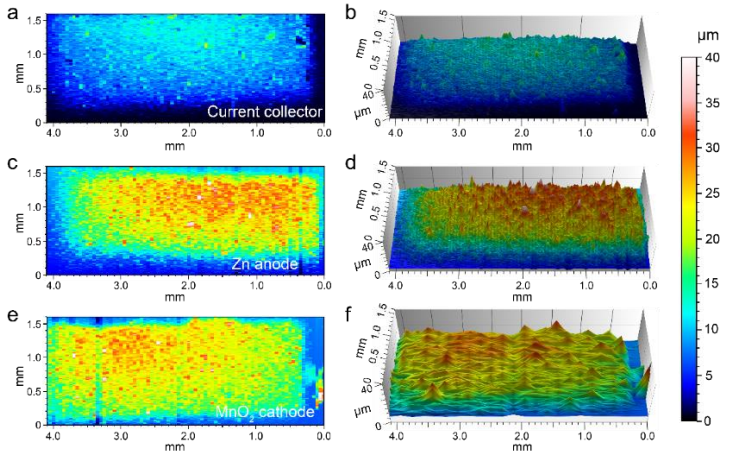

Figure S21. Two and three-dimensional surface thickness distribution of (**a**, **b**) carbon-based current collector, (**c**, **d**) Zn anode, and (**e**, **f**) MnO_2 cathode on PET substrate.

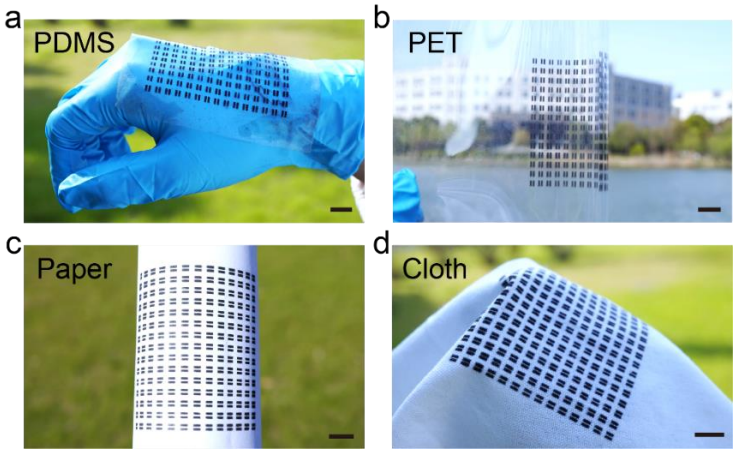

Figure S22. Photographs of the spray-printed planar MBs on various substrates. (**a**) PDMS film, (**b**) PET plate, (**c**) A4 paper, and (**d**) cloth. Scale bars, 1 cm.

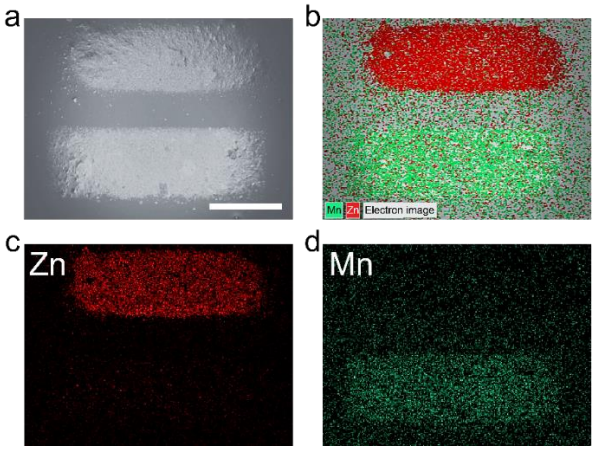

Figure S23. Scanning electron microscopic image of the printed electrodes and corresponding energy dispersive spectrometer mappings. Scale bar, 1 mm.

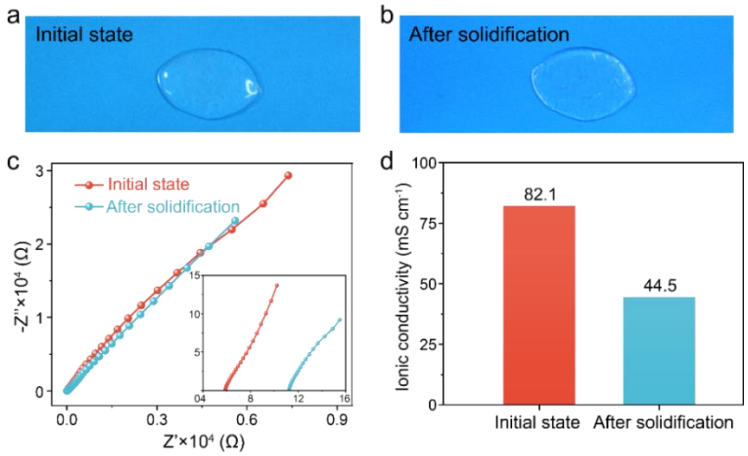

Figure S24. Optical photographs of the PVA-$ZnCl_2$/$MnSO_4$-LiCl gel electrolyte (**a**) at the initial state and (**b**) after solidification. (**c**) Nyquist impedance plots and (**d**) corresponding ionic conductivities at the initial state and after solidification.

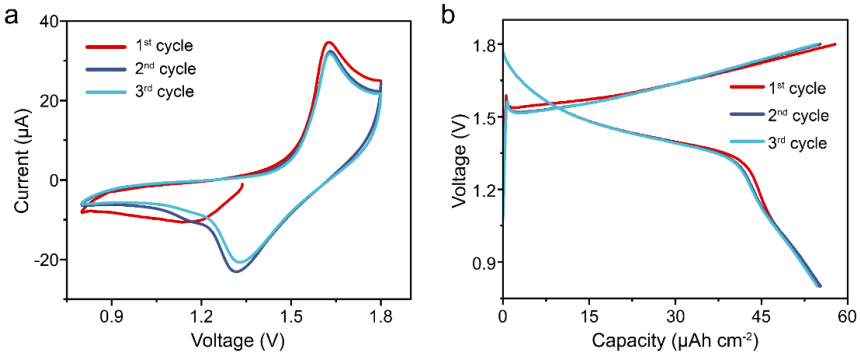

Figure S25. (**a**) Cyclic voltammetry curves at 0.2 mV s^{-1} and (**b**) galvanostatic charge-discharge curves at 50 μA cm^{-2} of the first three cycles of the Zn//MnO_2 MB.

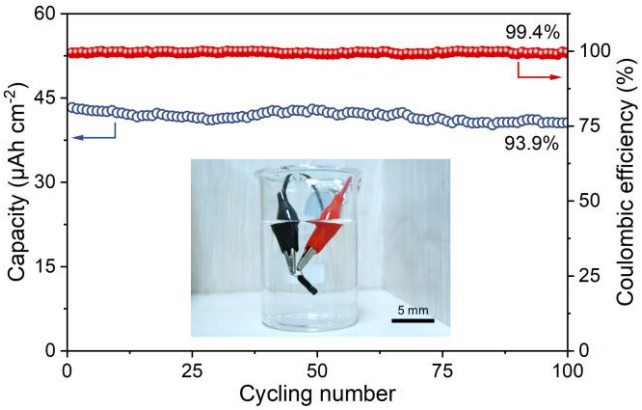

Figure S26. Areal capacity and Coulombic efficiency upon cycling at 80 μA cm^{-2} of an

encapsulated MB immersing in water.

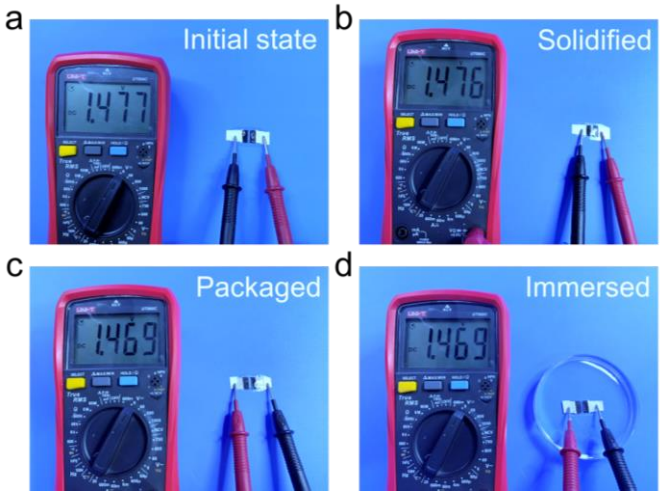

Figure S27. Open circuit voltages of the planar MB under different states. (**a**) Initial state, (**b**) after the gel electrolyte solidified, (**c**) after packaging, and (**d**) after immersing in water.

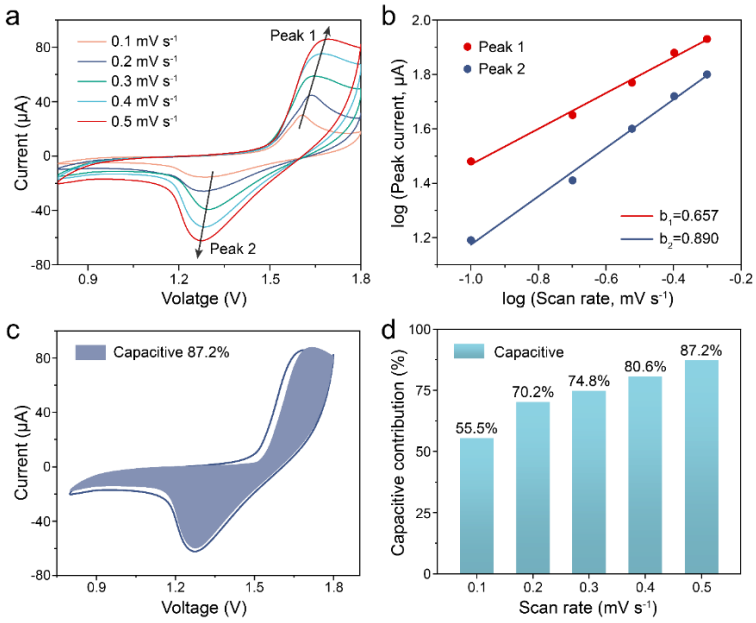

Figure S28. Electrode reaction kinetics analysis of the Zn//MnO_2 MB. (**a**) Cyclic voltammetry of the MB at scan rates ranging from 0.1 to 0.5 mV s^{-1}. (**b**) Plots of log(*i*) versus log(*v*) of the cathodic current response at the typical two peaks labeled in (**a**). (**c**) Cyclic voltammetry displaying the capacitive contribution to the total current at 0.5 mV s^{-1}. (**d**) Percentages of capacity contributions at increasing scan rates.

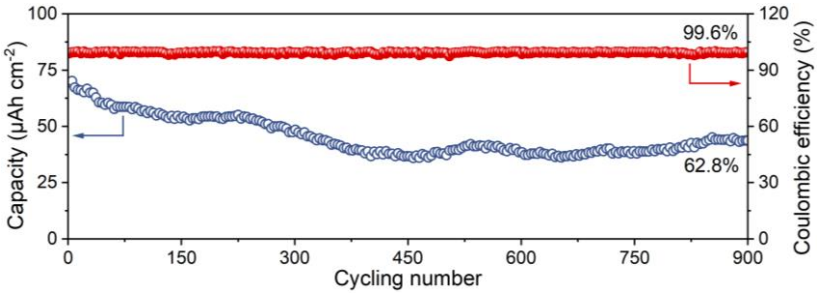

Figure S29. Cycling performance of Zn//MnO_2 MB at 50 μA cm^{-2} and corresponding Coulombic efficiency.

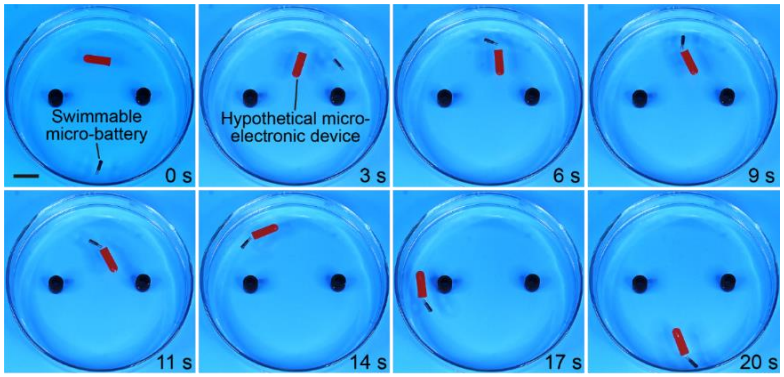

Figure S30. Experimental demonstration of the swimmable MB transporting a hypothetical microelectronic device (red). Scale bar, 1 cm.

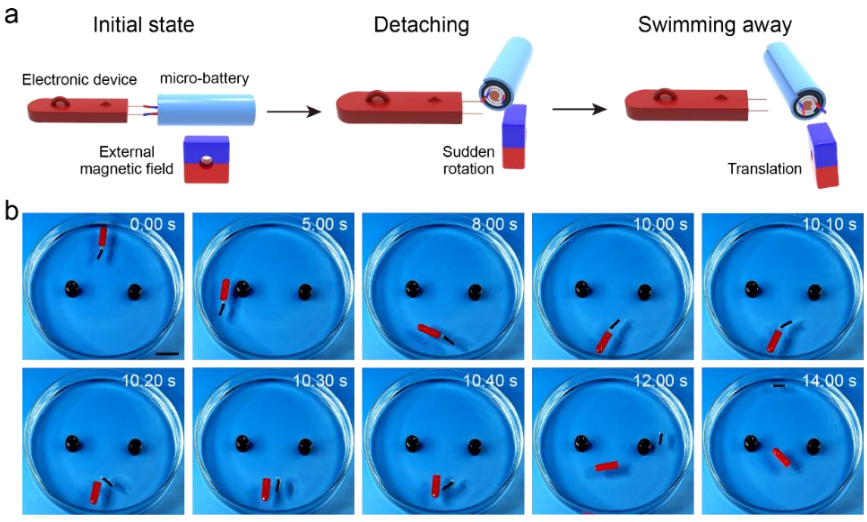

Figure S31. (**a**) A schematic diagram illustrating the detachment of the swimmable MB under the control of an external magnetic field. (**b**) Experimental demonstration of detaching the swimmable MB from a hypothetical electronic device (red). Scale bar, 1 cm.

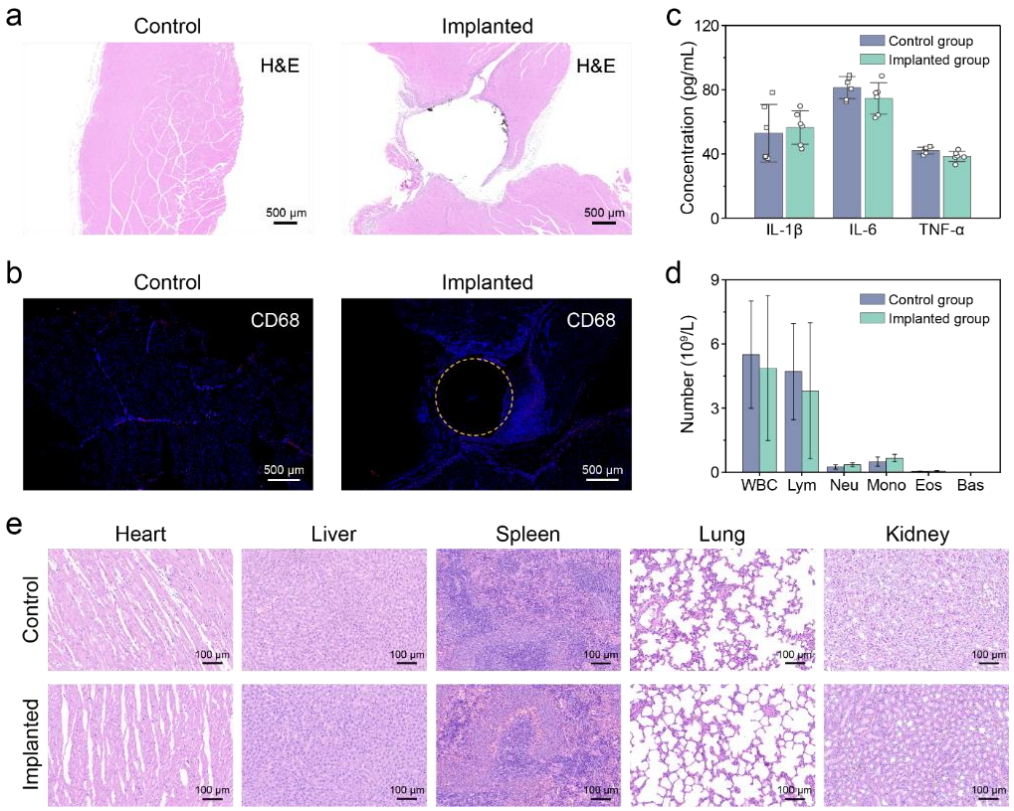

Figure S32. The biocompatibility of the swimmable micro-battery. (**a**, **b**) H&E and immunohistochemical staining images of rat tissue after one-week implantation of the swimmable micro-battery. The blue and red colors represent DAPI (a marker of the nucleus) and CD68 (a marker of macrophages), respectively. The orange dashed circle indicates the position of the swimmable MB. (**c**) Concentration of inflammatory factors (IL-1β, IL-6 and TNF-α) in rat serum after the swimmable MB implantation. (**d**) Results of the analysis of the inflammatory cells (WBC, Lym, Neu, Mono, Eos, and Bas) counts in rats with and without swimmable MB implantation. (**e**) H&E staining of the major organs of rats with and without implanted swimmable MB for one week.

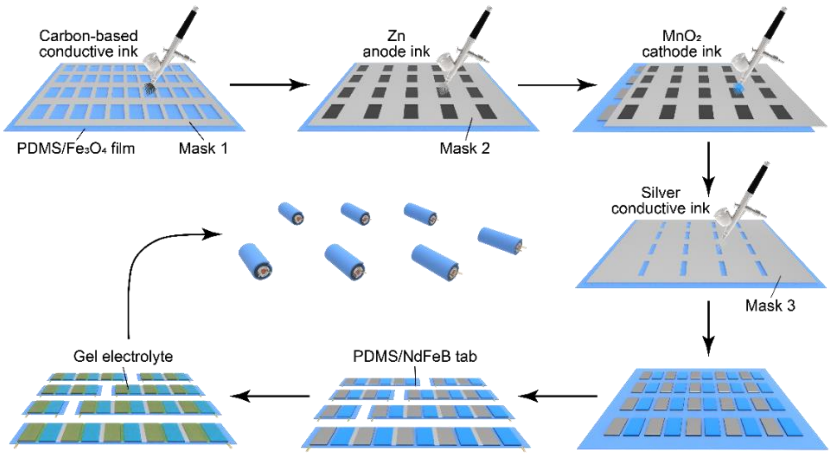

Figure S33. Schematic diagram of the preparation process for swimmable MBs in series.

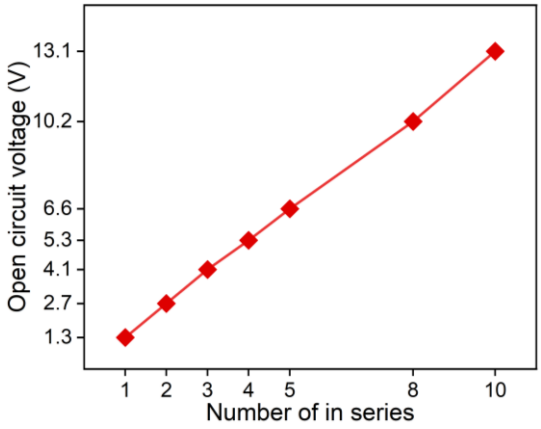

Figure S34. Dependence of the open circuit voltage on the number of MBs in series.

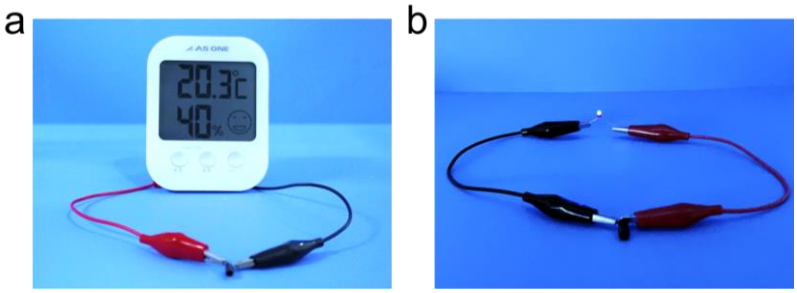

Figure S35. Photographs of the MB powering (**a**) a temperature and humidity meter and (**b**) a light-emitting dioxide.

Table S1. Electrochemical performance comparison of swimmable MBs with previously reported micro energy storage devices that were not swimmable.

Electrode material	Specific capacity	Energy density	Power density	Capacity retention	Volumetric energy density (full cell)	Ref.
Zn//MnO_2	102.3 μAh cm^{-2} at 10 μA cm^{-2}	141.9 μWh cm^{-2}	0.14 mW cm^{-2}	73% after 400 cycles	3.36 μWh cm^{-2}·μm^{-1} at 10 μA cm^{-2}	This work
Li//V_2O_5	0.15 mAh cm^{-2} at 1 C	1.24 J cm^{-2} at 1 C	75.5 mW cm^{-2}	75% after 200 cycles	-	[1]
LTO//LFP	14.5 mAh cm^{-2} at 0.2 mA cm^{-2}	20 mWh cm^{-2} at 0.2 mA cm^{-2}	-	>60% after 100 cycles at 0.2 mA	-	[2]
ZnO@MnO_2	26 mF cm^{-2} at 0.5 mA cm^{-2}	-	2.44 mW cm^{-3}	87.5% after 10000 cycles at 0.5 mA	3.5 mWh cm^{-3} at 0.5 mA cm^{-2}	[3]
Zn//MnO_x@ polypyrrole	110 μAh cm^{-2} at 0.2 mA cm^{-2}	360 Wh kg^{-1} at 0.2 mA cm^{-2}	33 mW cm^{-3}	95% after 200 cycles	21 mWh cm^{-3} at 33 mW cm^{-3}	[4]
Reduced graphene	80.7 μF cm^{-2} at 1000 V s^{-1}	-	495 W cm^{-3}	98.3% after 100000 cycles at 50 V s^{-1}	2.5 mWh cm^{-3}	[5]
LMO//NiSn	-	-	7.4 mW cm^{-2} $μm^{-1}$	64% after 15 cycles	15 μW h cm^{-2}·$μm^{-1}$	[6]
Zn//PANI	40.48 μAh cm^{-2} at 330 mA cm^{-3}	32.0 μWh cm^{-2}	1.86 mW cm^{-2}	56.7% after 500 cycles at 660 mA	-	[7]
PPyNW	8.15 mF cm^{-2} at 0.2 mA cm^{-2}	-	0.89 W cm^{-3}	~96% after 20000 cycles at 1 mA cm^{-2}	15.25 mWh cm^{-3} at 0.89 W cm^{-3}	[8]
NiSn//$LiMnO_2$	2.9 μAh cm^{-2}·$μm^{-1}$ at 1 C	-	3,600 μW cm^{-2} · $μm^{-1}$	77% after 200 cycles	6.5 μWh cm^{-2}·$μm^{-1}$ at 1 C	[9]
$NaTi_2(PO_4)_3$@C// $Na_{0.44}MnO_2$	43 mAh g^{-1} at 0.1 A g^{-1}	0.47 mWh cm^{-2}	3.8 W cm^{-3}	60% after 1000 cycles at 0.2 A g^{-1}	23.8 mWh cm^{-3} at 0.1 A g^{-1}	[10]

Supporting Note S1. Electrode reaction kinetics study of the quasi-solid-state Zn//MnO_2 MB.

Figure S28 (**a**) displayed the cyclic voltammetry curves of the quasi-solid-state Zn//MnO_2 MB at different scan rates (0.1, 0.2, 0.3, 0.4, and 0.5 mV s^{-1}) within a voltage window from 0.8 to 1.8 V. The relationship between the peak current density (*i*) and scan rate (*v*) was assumed to follow the equation: $i=a\cdot v^b$,

which could also be rearranged as: $log(i)=blog(v) + log(a)$,

where *a* and *b* are adjustable constants, *b* could be viewed as the slope of *log(i)* versus *log(v)* curve. When *b* approaches 0.5, a sluggish faradic intercalation dominates the process; when the b value is close to 1.0, a fast capacitive control is indicated.[11] After fitting the two charge/discharge peaks, the *b* values of Peak 1 and 2 in cyclic voltammetry curves are calculated to be 0.657 and 0.890, respectively (**Figure S28** (**b**)), suggesting that the Zn//MnO_2 MB are synchronously controlled by the ionic diffusion and pseudocapacitance process.

Furthermore, the quantitative capacitive contributions were analyzed by separating the current (*i*) at a fixed potential (V) into capacitive effect (k_1v) and diffusion-controlled insertion ($k_2v^{1/2}$), using the equation: $i=k_1v + k_2v^{0.5}$

which could also be represented as: $i/v^{0.5} =k_1v^{0.5} + k_2$

where *i*, k_1v, and $k_2v^{0.5}$ represented the current response, capacitive, and ionic diffusion-controlled contributions, respectively.[12] **Figure S28** (**c**) depicted the cyclic

voltammetry profile at a scan rate of 0.5 mV s^{-1} for the capacitive current (blue region) compared with the total current in the Zn//MnO_2 MB with a capacitive contribution of 87.2%. Upon decreasing scan rates, the percentages of capacitive contribution accordingly decreased to 80.6%, 74.8%, 70.2%, and 55.5% at scan rates of 0.4, 0.3, 0.2, and 0.1 mV s^{-1}, respectively (**Figure S28** (**d**)). These results indicated that the Zn//MnO_2 MB showed facilitated electrode reaction kinetics.

References

[1] P. Sun, X. Li, J. Shao, P. V. Braun, *Adv. Mater.* **2021,** *33*, 2006229.

[2] T. Wei, B. Y. Ahn, J. Grotto, J. A. Lewis, *Adv. Mater.* **2018,** *30*, 1703027.

[3] P. Yang, X. Xiao, Y. Li, Y. Ding, P. Qiang, X. Tan, W. Mai, Z. Lin, W. Wu, T. Li, H. Jin, P. Liu, J. Zhou, C. P. Wong, Z. L. Wang, *ACS Nano* **2013,** *7*, 2617.

[4] M. Zhu, Z. Wang, H. Li, Y. Xiong, Z. Liu, Z. Tang, Y. Huang, A. L. Rogach, C. Zhi, *Energy Environ. Sci.* **2018,** *11*, 2414.

[5] Z. S. Wu, K. Parvez, X. Feng, K. Müllen, *Nat. Commun.* **2013,** *4*, 2487.

[6] J. H. Pikul, H. Gang Zhang, J. Cho, P. V. Braun, W. P. King, *Nat. Commun.* **2013,** *4*, 1732.

[7] S. Bi, F. Wan, S. Huang, X. Wang, Z. Niu, *ChemElectroChem* **2019,** *6*, 3933.

[8] M. Zhu, Y. Huang, Y. Huang, H. Li, Z. Wang, Z. Pei, Q. Xue, H. Geng, C. Zhi, *Adv. Mater.* **2017,** *29*, 1605137.

[9] H. Ning, J. H. Pikul, R. Zhang, X. Li, S. Xu, J. Wang, J. A. Rogers, W. P. King, P. V. Braun, *Proc. Natl. Acad. Sci. USA* **2015,** *112*, 6573.

[10] Z. Guo, Y. Zhao, Y. Ding, X. Dong, L. Chen, J. Cao, C. Wang, Y. Xia, H. Peng, Y. Wang, *Chem* **2017,** *3*, 348.

[11] X. Pu, D. Zhao, C. Fu, Z. Chen, S. Cao, C. Wang, Y. Cao, *Angew. Chem. Int. Ed.* **2021,** *60*, 21310.

[12] Y. Zhao, R. Zhou, Z. Song, X. Zhang, T. Zhang, A. Zhou, F. Wu, R. Chen, L. Li, *Angew. Chem. Int. Ed.* **2022,** *61*, e202212231.